1 **Supporting Information**

2 **Dynamically Activating Ni-Based Catalysts by Self-Anchored**

3 **Mononuclear Fe for Efficient Water Oxidation**

4

5 Zhiyuan Zhang[1,6], Yuting Luo[1,4,6], Kun Wang[1,6], Qiangmin Yu[1], Xin Kang[1], Yingqi Liu[1],

6 Ke Xie[4], Zhengxing Lv[2], Zhibo Liu[3], Fengning Yang[1], Heming Liu[1], Ke Liu[2], Jiong Li[2],

7 Guangmin Zhou[1], Wencai Ren[3], Hui-Ming Cheng[1,3,5], Jia Li*[1], Shuo Zhang*[2] & Bilu

8 Liu*[1]

9 [1]Shenzhen Geim Graphene Center, Tsinghua-Berkeley Shenzhen Institute & Institute of

10 Materials Research, Tsinghua Shenzhen International Graduate School, Tsinghua

11 University, Shenzhen 518055, P. R. China.

12 [2]Shanghai Synchrotron Radiation Facility, Shanghai Advanced Research Institute,

13 Chinese Academy of Sciences, Shanghai 201210, China.

14 [3]Shenyang National Laboratory for Materials Sciences, Institute of Metal Research,

15 Chinese Academy of Sciences, Shenyang, Liaoning 110016, P. R. China

16 [4]Department of Electrical and Computer Engineering, University of Toronto, 35 St

17 George Street, Toronto, Ontario M5S 1A4, Canada.

18 [5] Shenzhen Institute of Advanced Technology, Chinese Academy of Sciences, Shenzhen

19 518055, China.

20 [6]These three authors contributed equally.

21 * E-mail: bilu.liu@sz.tsinghua.edu.cn; zhangshuo@sinap.ac.cn; li.jia@sz.tsinghua.edu.cn

1 This file contains description of experimental and calculation methods, 15 Supplementary

2 Figures, and 8 Tables.

3

4 **Methods**

5 **Chemicals.** Nickel (II) nitrate hexahydrate (with a formula of $Ni(NO_3)_2 \cdot 6H_2O$, AR,

6 Guangdong Guanghua Sci-Tech Co., Ltd, China), ammonium molybdate tetrahydrate

7 (with a formula of $(NH_4)_6Mo_7O_{24} \cdot 4H_2O$, AR, Shanghai Aladdin Biochemical Technology

8 Co., Ltd, China), and potassium hydroxide (KOH, AR, Shanghai Macklin Biochemical

9 Co., Ltd, China) were used without further purification. Ni foams (0.5 mm thick, purity

10 >99.99%, Linyi Gelon LIB Co., Ltd, China) were used as received. Ultrapure Direct-Q

11 water (18.2 $M\Omega$ cm^{-1}) was used to prepare all the aqueous solutions and for washing

12 samples.

13

14 **Synthesis of Fe-doped $NiMoO_4$.** Fe-doped $NiMoO_4$ on Ni foam was synthesized by a

15 hydrothermal method. First, a piece of Ni foam (40 mm × 10 mm × 0.5 mm) was sonicated

16 in a 1 M HCl aqueous solution for 40 min to remove the surface oxide layer and then

17 washed with deionized water to remove residual HCl. Second, $(NH_4)_6Mo_7O_{24}$ (0.3 mol),

18 $Ni(NO_3)_2 \cdot 6H_2O$ (1.2 mmol), and $Fe(NO_3)_3 \cdot 9H_2O$ (0.075 mmol) were added to deionized

19 water (30 mL) and stirred to form a uniform solution. Finally, the mixed solution and the

20 cleaned Ni foam were transferred into a 100 mL Teflon-lined stainless-steel autoclave for

21 the hydrothermal reaction at 120 °C for 12 h. The prepared Fe-doped $NiMoO_4$ on Ni foam

1 was thoroughly washed with deionized water and then dried in a vacuum at 60 °C for 12

2 h.

3

4 **Synthesis of Fe$_1$-NiMo**. Fe$_1$-NiMo was synthesized by H$_2$ reduction of Fe-doped NiMoO$_4$.

5 The hydrothermal prepared Fe-NiMoO$_4$ was put into a quartz tube furnace. The tube was

6 firstly purged with Ar (400 sccm) for 30 min and then heated up to 500 °C at a rate of 8 °C

7 min^{-1}. The mixture of Ar (190 sccm.) and H$_2$ (10 sccm) was then introduced for 30 min to

8 prepare the Fe$_1$-NiMo catalyst. After that, H$_2$ was turned off and the furnace was cooled to

9 room temperature under Ar (190 sccm). For the NiMo control samples, the synthetic

10 procedures were the same as that of the Fe$_1$-NiMo catalyst, but the Fe precursors were not

11 added into the solution in the hydrothermal growth step.

12

13

14 **Materials characterization.** The morphology of the samples was examined by SEM (5

15 kV, Hitachi SU8010, Japan). HRTEM analyses were carried out at an electron acceleration

16 voltage of 300 kV (FEI Titan Cubed Themis G2 300, USA). Structural and chemical

17 analyses of the samples were performed by powder XRD (Cu Kα radiation, λ=0.15418 nm,

18 Bruker D8 Advance, Germany). High-resolution XPS was performed with Al Kα X-rays

19 (PHI5000VersaProbeII, Japan, and ESCALAB 250Xi, USA). The XPS profile was

20 performed by Ar etching with an accelerating voltage of 4 kV and an angle of 45°. The

21 element content was tested by ICP-OER (SPECTRO Arcos II MV, Germany). The

1 reconstructed sample for postmortem characterization (SEM, HRTEM, ICP-OES, and

2 XPS) experienced an OER process at a current density of ~100 mA cm^{-2} for 100h. The

3 sample named OC was immersed in oxygen saturated 1M KOH solution for 30 min. The

4 reconstructed samples for characterization were taken out from the electrolyte, then washed

5 with water, and finally dried in a vacuum drier. The transfer procedure was finished within

6 one minute.

7

8 **In-situ XAS measurements.** The XAS spectra at the Fe and Ni K-edges were recorded at

9 the BL11B beamline of the Shanghai Synchrotron Radiation Facility (SSRF). The beam

10 current of the storage ring was 220 mA in a top-up mode. The incident photons were

11 monochromatized by a Si (111) double-crystal monochromator, with an energy resolution

12 $\Delta E/E$ ~1.4×10^{-4}. The spot size at the sample was ~200 μm × 250 μm (H × V). The XAS

13 spectra of the samples at Fe and Ni K-edges were calibrated by the Fe and Ni reference

14 foils, respectively. The Fe$_1$-NiMoFe catalyst powders were exfoliated from Ni foam

15 supports and then loaded on carbon papers. In-situ XAFS measurements were performed

16 with the carbon paper as a working electrode using a homemade in-situ electrochemical

17 cell setup. A graphite rod was used as a counter electrode and a double-salt-bridge saturated

18 calomel electrode (SCE) as a reference electrode in 1.0 M KOH solution. Electrochemical

19 measurements were conducted on CHI 660E electrochemical workstation. XAFS

20 measurement was carried out after potential was for 10 min. In-situ XAFS spectra at the

21 Ni and Fe K-edges were collected in fluorescence mode, with a Lytle ionization chamber

1 filled with Ar. Ni and Fe K edges of references are collected in transition mode.

2 **XAFS data analysis.** The data of XAFS were processed with ATHENA software

3 implemented in the IFEFFIT software packages.[1] The raw data of XAFS were background

4 subtracted from the overall absorption and then normalized regarding the edge-jump step.

5 Next, the k^3-weighted $\chi(k)$ data of Fe K-edge and Ni K-edge were Fourier transformed to

6 R space using a Hanning window (dk = 1.0 Å^{-1}) in k-space, which separates the

7 contributions of different coordination shells to the EXAFS data. EXAFS of Fe K-edge

8 were Fourier transformed between 2.670 and 12.085 Å^{-1}. And EXAFS data Ni K-edge were

9 Fourier transformed between 2.556 and 12.335 Å^{-1}. The quantitative structure parameters

10 of Fe were obtained by least-squares fitting of EXAFS data with ATERMIS software in

11 the IFEFFIT software packages. The fitting was according to the EXAFS equation:

$$\chi(k) = \sum_i \frac{N_i S_0^2 F_i(k)}{kR_i^2} \sin\left(2kR_i + \varphi_i(k)\right) e^{\frac{-2R_i}{\lambda(k)} -- 2\sigma_i^2 k^2}$$

12

13 where $F_i(k)$, the effective scattering amplitude, $\lambda(k)$ the mean free path, and $\varphi_i(k)$, the

14 effective scattering phase shift were theoretically calculated by the ab-intio code FEFF 6[2].

15 The fitting was conducted in R space with the single scattering path of the first and the

16 second coordination shells. The multiple scattering paths are not considered in our fitting

17 since the noise of the in-situ EXAFS data is relatively high. The fitting in R space is more

18 reasonable than in k space in this work because we cannot use all the path in the EXAFS

19 fitting.

20   The wavelet transformations of EXAFS were performed in the k range between 2.65

5

1 and 12.10 Å^{-1} with a k step of 0.05 Å^{-1} and the R range between 0 and 6 Å with the

2 hamaFortran program by using the Morlet wavelets[3]:

$$\varphi(k) = \frac{1}{\sqrt{2\pi}\sigma} e^{-\frac{k^2}{2\sigma^2}} (e^{i\omega k} - e^{-\frac{k^2}{2}})$$

4 Where ω is the frequency and σ is the half width. We chose ω=6 and σ=0.83 to get a high

5 resolution in the region of the second coordination shell of pristine Fe$_1$-NiMo and Fe$_1$-

6 NiMo under OC conditions. The wavelet transformation of EXAFS of Fe$_1$-NiMo at 1.47

7 V vs RHE is performed with ω=5 and σ=1.2.

8

9 **In-situ XRD measurements.** The XRD measurements were conducted with a synchrotron

10 radiation X-ray beam (16 keV) at the BL17U beamline of the Shanghai Synchrotron

11 Radiation Facility (SSRF). The working electrode for in-situ XRD measurement was

12 prepared by the following two step. In the first step, we exfoliated catalyst powders and

13 collected them. We put a piece of Ni foam loading Fe$_1$-NiMo in a polypropylene tube and

14 shook the tube violently, then some powders falling off from the Ni foam was collected. A

15 magnate was then used to separate the fragments of Ni foam from Fe$_1$-NiMo in the

16 powders. The exfoliation and collection processes were done in a glove box filled with Ar

17 gases. In the second step, we prepare the working electrode for in-situ XRD. 10 mg of Fe$_1$-

18 NiMo powers were dispersed in 1 mL isopropanol under sonication and formed a uniform

19 ink. Then, 400 μL ink was gradually dropped on carbon paper (1.5 cm $\times$ 1.5 cm) for the

20 in-situ XRD measurement. In-situ XRD measurements were performed with the carbon

paper as a working electrode using a homemade in-situ electrochemical cell setup. A

graphite rod was used as a counter electrode and a mercuric oxide electrode as a reference

electrode in 1 M KOH solution. The electrode potential was set as 0.7 V vs Hg/HgO

reference. The reflection patterns were collected by a plane detector (Dectris Eiger 16M,

E-32-0111) with an exposure time of 1 s and an exposure period of 1 s.

In-situ Raman measurements. Raman spectra were collected using a 633 nm laser

excitation with a beam size of ~1 μm grating (Horiba LabRAB HR800, Japan). Catalyst

powders were exfoliated from Ni foam and then were loaded on a Ti foil whose surface is

coated gold by E-beam evaporation. In-situ Raman measurements were performed with the

gold-coated Ti foil that was loaded with catalysts as a working electrode using a homemade

in-situ electrochemical cell setup. A Pt wire was used as a counter electrode and a double

salt bridge SCE as a reference electrode in 1 M KOH solution. The scattered light was

collected by a 50 X objective lens and then directed to a charge-coupled device (CCD)

detector. Before in-situ experiments, the monochromator was calibrated by 520.7 cm^{-1}, the

peak of silicon.

Electrochemical measurements. The mass loading of the Fe_1-NiMo and NiMo catalyst

were measured to be 3.7 mg cm^{-2} and 8.4 mg cm^{-2} respectively. IrO_2 with a mass loading

of ~4 mg cm^{-2} was drop-casted on Ni foam as a comparison sample. The Ni foam loaded

IrO_2 was annealed in Ar at 500 °C before the electrochemical test. A standard three-

1 electrode electrolyzer with oxygen-saturated KOH (1.0 M) was used in all tests, a double-

2 salt-bridge SCE as reference electrodes and a graphite rod as counter electrodes. The scan

3 rate was 1 mV s^{-1} for cyclic voltammetry tests. The cyclic voltammetry test was tested

4 repeatedly before stable and the final data were reported. To eliminate the signal from the

5 oxidation of Fe and Ni, the negatively scanned polarization curves were used. For fair

6 comparisons, an 85% iR correction was taken. The distance between the reference

7 electrode and the working electrode was fixed by a capillary filling with saturated KCl

8 solutions. And the SCE is immersed in this capillary, constituting a double salt bridge

9 setup. The double-salt-bridge SCE was used as reference electrode in all the tests except

10 in-situ XRD measurements. Faradaic efficiencies were defined as the ratio of O_2 volume

11 collected in an experiment to the volume in theory, and O_2 was collected by the water

12 drainage method. Stability tests were performed by the chronoamperometry measurements

13 method.

14   To get specific activity, the reaction current was normalized by the electrochemical

15 surface area (ECSA) of catalysts. ECSA was calculated by ECSA= $\dfrac{C_{dl}}{C_s}$, where C_{dl} is the

16 electrochemical double-layer capacitance of working electrodes and C_s is specific

17 capacitance of the electrode materials, which was recommended as 0.04 mF cm^{-2} in

18 alkaline[4, 5]. Considering the reconstruction of catalysts, the electrochemical double-layer

19 capacitance was tested after the OER process. The specific activity normalized by the

20 redox-active sites was also provided, where the reducing reactions is assumed as a single

electron reaction and all the metal atoms that participated in the reducing reaction are

assumed the active sites. The number of redox-active (m_{redox}) sites was calculated

according to the area of reducing peak according to $m_{redox} = \dfrac{\int \dfrac{j(E)}{v} A dE}{nF}$, where j is the

current density, E is the electrode potential, v is the scan rate, A the geometric surface area

of working electrodes, F is the Faraday constant (96485 C mol^{-1}), and n is the number of

electrons involved in the reaction.

TOF was calculated by TOF $= \dfrac{j \times A}{4 \times F \times m}$. In this study, we assumed all metal atoms,

including Ni, Fe, Mo, and Ir, in catalysts are counted as active sites to avoid overwhelming

of activity of catalysts, and the amounts of metal elements of Fe$_1$-NiMo and NiMo were

obtained by ICP-OES (Table S8). TOF based on m_{redox} was also provided.

Membrane electrode assembly measurement. The membrane electrode measurement

was performed in a homemade step (Figure S14) under ambient temperature and pressure

with Fe$_1$-NiMo catalysts grown on Ni foam as the anode and commercial Pt/C catalysts as

the cathode. A Pipnioer anion exchange membrane was used to separate the anode and the

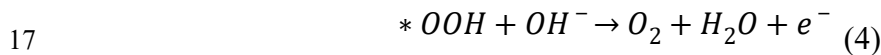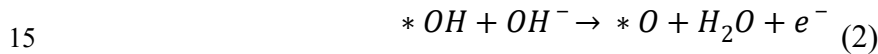cathode chambers. The flow rate of anolyte is about 40 mL min^{-1}.

DFT calculations.

All DFT calculations were performed by the Vienna Ab initio Simulation Package

1 (VASP).[6-8] The generalized gradient approximation (GGA) of the Perdew-Burke-

2 Ernzerhof (PBE) functional[9] and the projector augmented-wave (PAW) potential[10] were

3 employed. Grimme method[11, 12] was used to consider the van der Waals' interaction for

4 layer materials. The GGA + U calculations were performed using the model proposed by

5 Dudarev et al.,[13] with the effective U values of 6.4, and 4.0 eV for Ni and Fe, respectively.

6 The layered oxyhydroxide monolayers were constructed by using a 4 × 4 supercell. The

7 constructed supercell was isolated with a 15 Å vacuum space in the z-direction. For all

8 geometry optimizations, the cutoff energy was set to 520 eV. Monkhorst–Pack grids (3 ×

9 3 × 1) were used to sample the Brillouin zones of the supercell. The force and energy

10 convergence criterion were set to be 2×10^{-2} eV $Å^{-1}$ and 10^{-5} eV, respectively. The (001)

11 facet of NiOOH is used in calculations because it is considered to be energetically

12 favorable to absorbing water molecules and forming the electrode-solution interface.[14]

13   In alkaline conditions, OER can occur via the following four elementary steps:

$$* \ + OH^- \rightarrow *OH + e^- \quad (1)$$

$$*OH + OH^- \rightarrow *O + H_2O + e^- \quad (2)$$

$$*O + OH^- \rightarrow *OOH + e^- \quad (3)$$

$$*OOH + OH^- \rightarrow O_2 + H_2O + e^- \quad (4)$$

18 where * denotes the active sites on the catalyst surface. The computational hydrogen

19 electrode (CHE) [15, 16] was used to calculate the free energies of intermediates. The free

20 energy of an adsorbed species is defined as

21 $\Delta G = \Delta E + \Delta ZPE - T\Delta S \quad (5)$

1 where ΔE is the electronic adsorption energy, ΔZPE is the zero-point energy difference

2 between adsorbed and gaseous species, and $T\Delta S$ is the corresponding entropy difference

3 between these two states.

4
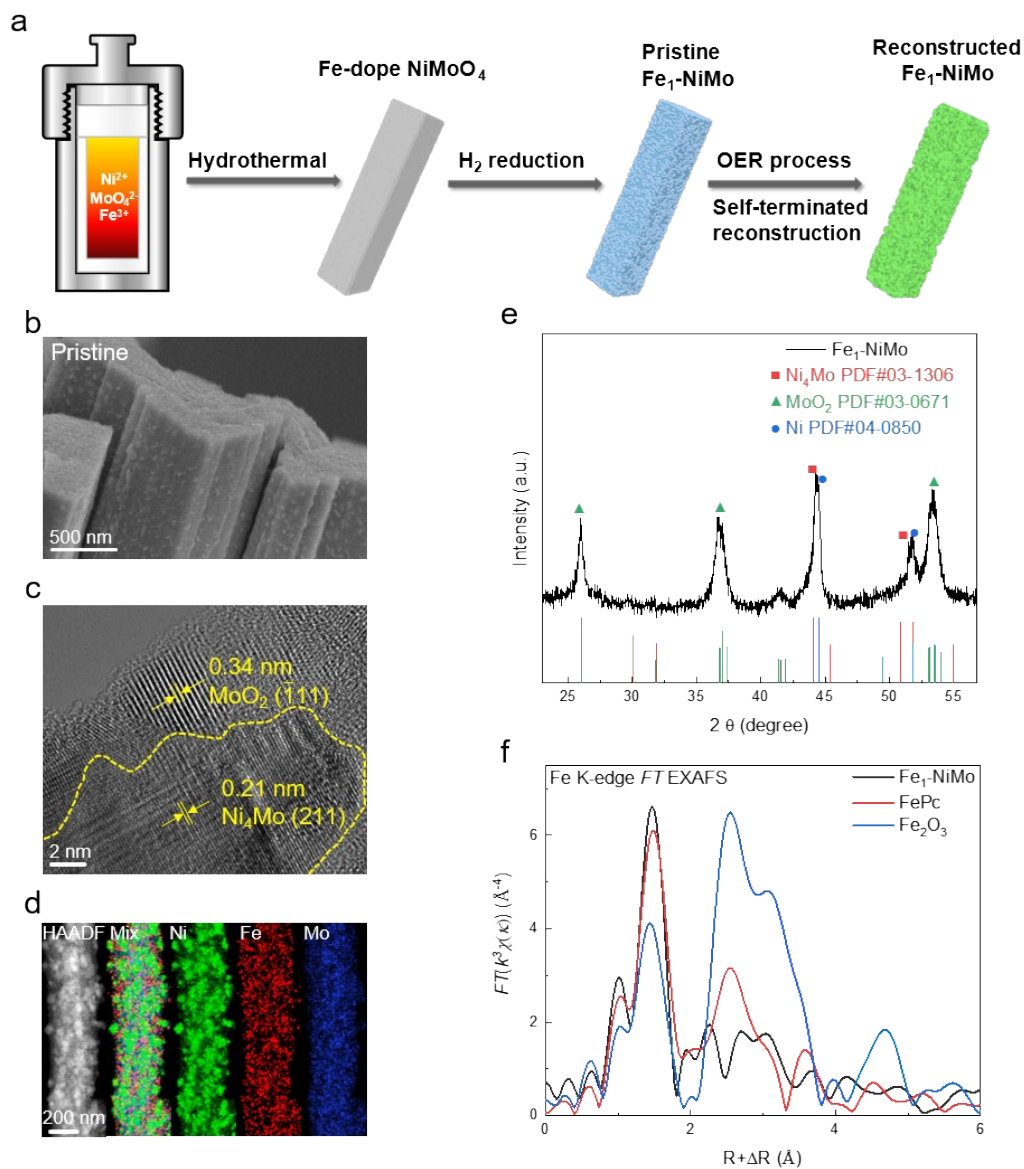
**Figure S1.** Synthesis and characterization of the Fe_1-NiMo catalyst. (a) Synthesis

6 flowchart and morphology evolution process of the Fe_1-NiMo. (b-e) SEM image (b),

7 HRTEM image (c), and EDS mapping (d), and (e) PXRD pattern Fe_1-NiMo before

1 immersed into KOH electrolyte. The results indicate that the Fe_1-NiMo composed of

2 Ni_4Mo nanoparticles and MoO_2 prisms. For short, it is denoted as Fe_1-NiMo in this work.

3 f, FT-EXAFS at Fe K-edge of pristine Fe_1-NiMo and Fe_2O_3 reference, demonstrate that Fe

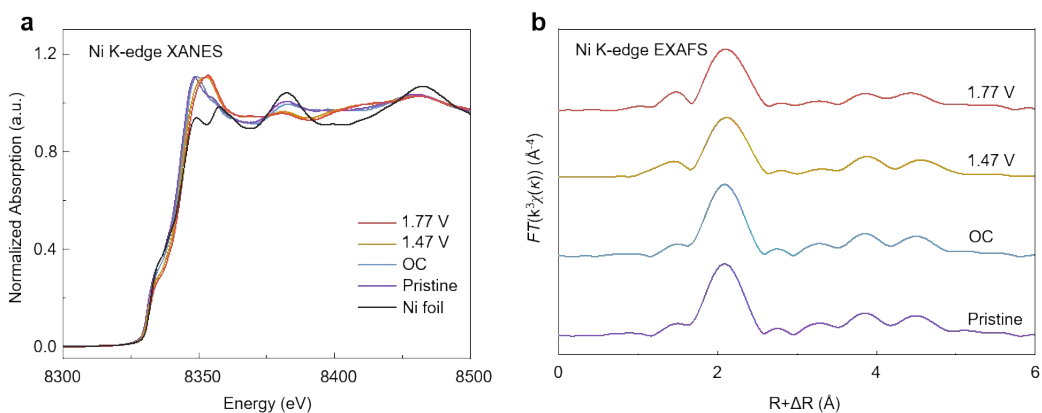4 in pristine Fe_1-NiMo exist as mononuclear metal center species.

5
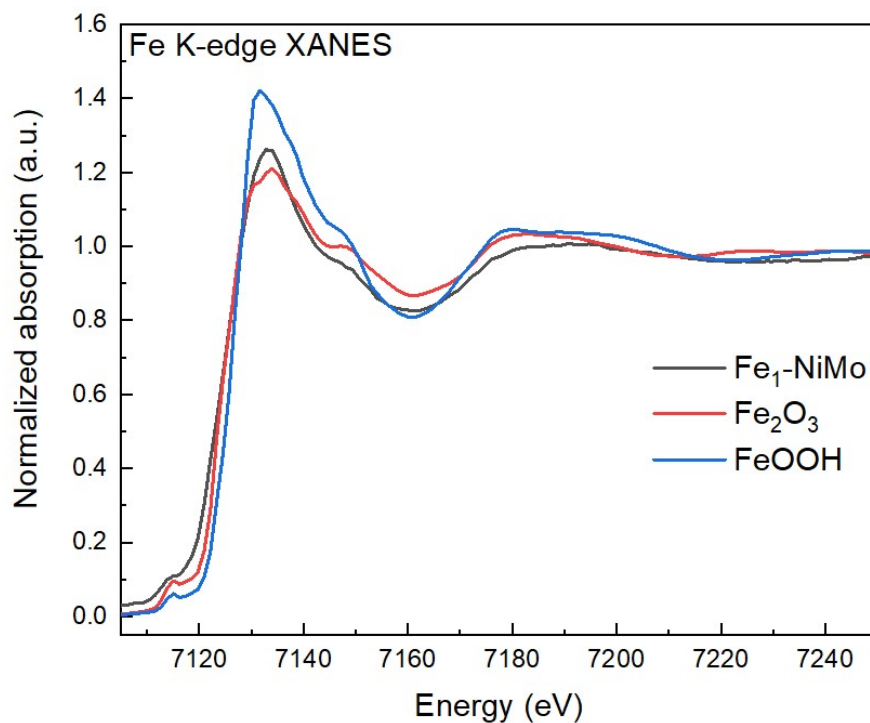
6

7 **Figure S2. Comparison of XANES at Fe K-edge of Fe_1-NiMo and contrasts.** These

8 results shows that Fe in Fe_1-NiMo is not locate in isolated phase.

9

1
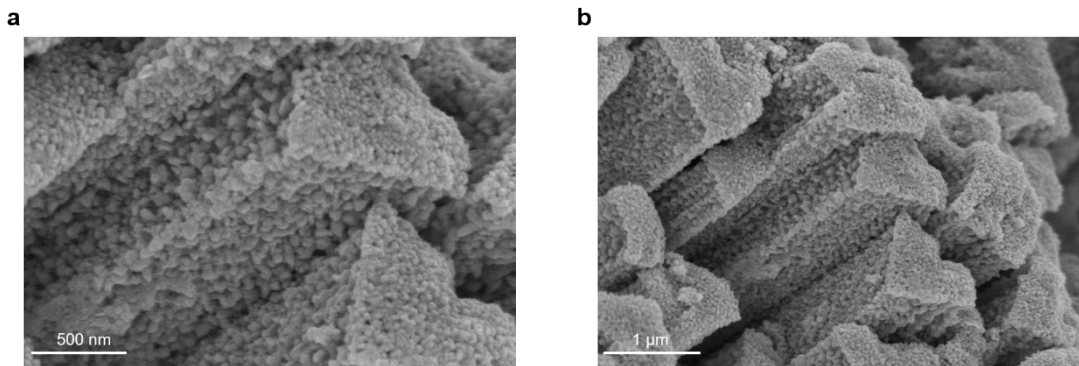
Figure S3. SEM images of the reconstructed Fe$_1$-NiMo. These images indicate the

reconstructed catalyst is assembled by nanoparticles.

4
5

6

Figure S4. In-situ XAFS of the Fe$_1$-NiMo at the Ni K-edge. XANES (a), FT-EXAFS (b),

of Fe$_1$-NiMo under ex-situ condition (pristine) and OER condition (from OC to 1.77 V *vs*

RHE in 1 M KOH). These results state that Ni mainly maintains metallic state under OER

condition.

11
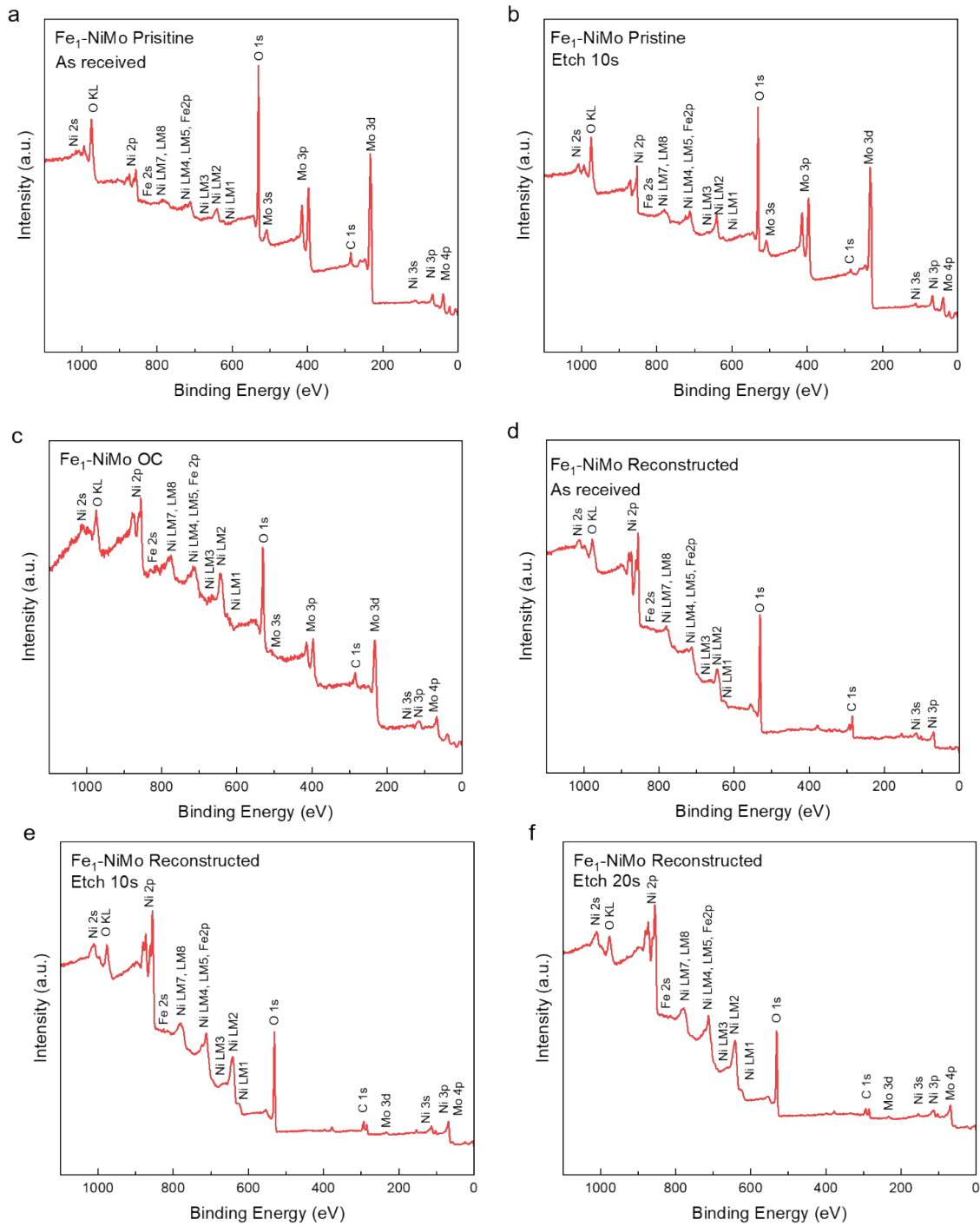
Figure S5. XPS survey spectra of Fe$_1$-NiMo. The pristine Fe$_1$-NiMo(a), and Fe$_1$-NiMo etched with Ar ions for 10s (b), Fe$_1$-NiMo after OC (c), Fe$_1$-NiMo after reconstructed under OER (d), reconstructed Fe$_1$-NiMo etched with Ar ions for 10 s (e), and reconstructed Fe$_1$-NiMo etched with Ar ions for 20 s (f). The rate of etching is ~ 0.2 nm s^{-1}. Fe 2p peaks are

1 overlapped with Ni LM4 and Ni LM5.
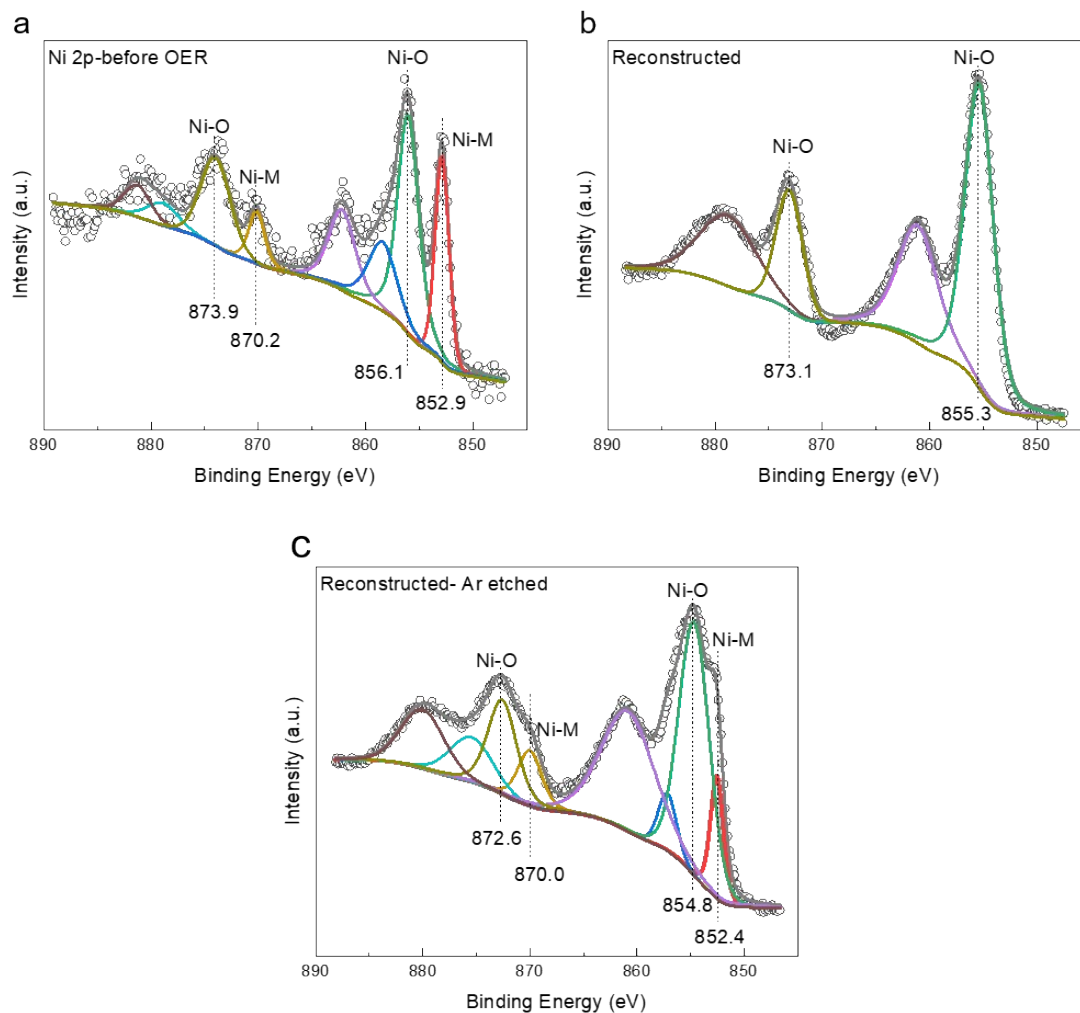
Figure S6. Ni *2p* XPS of pristine Fe₁-NiMo (a), reconstructed Fe₁-NiMo (b), and Ar ions etched reconstructed Fe₁-NiMo (c). The metallic Ni disappeared in reconstructed Fe₁-NiMo but arise after etched by Ar ions. The peak positions of main lines are marked below the spectra.
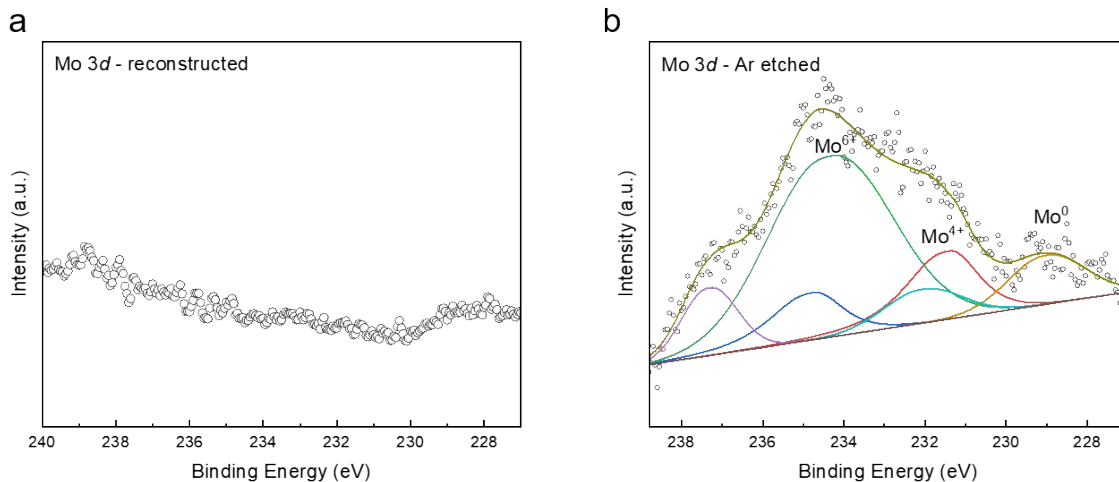
Figure S7. Mo *3d* XPS of the reconstructed Fe$_1$-NiMo (a), and reconstructed Fe$_1$-NiMo etched by Ar ions for 10 s (b). The signal of Mo 3*d* is not detected in the reconstructed surface, but appears after Ar ions etching.
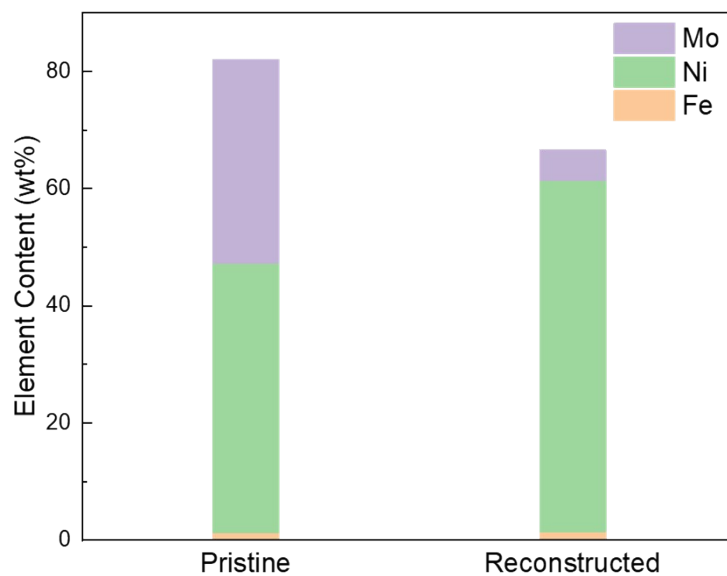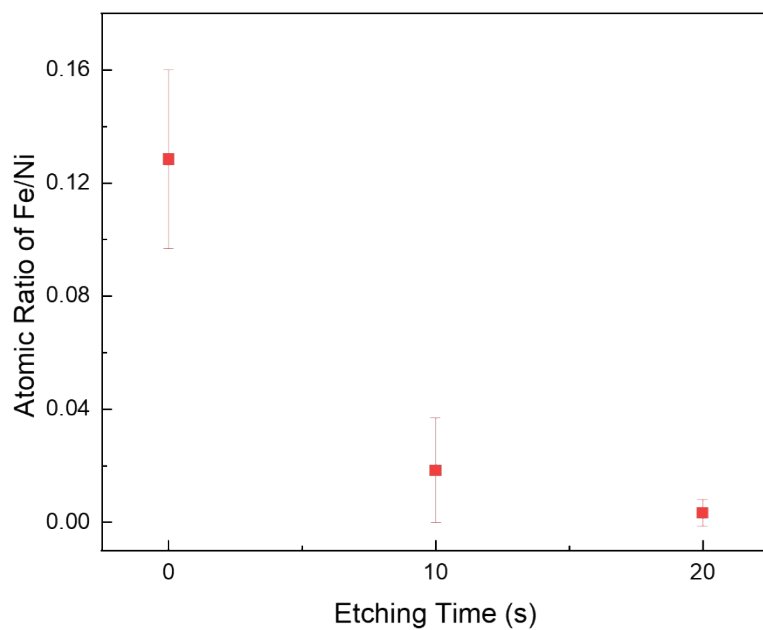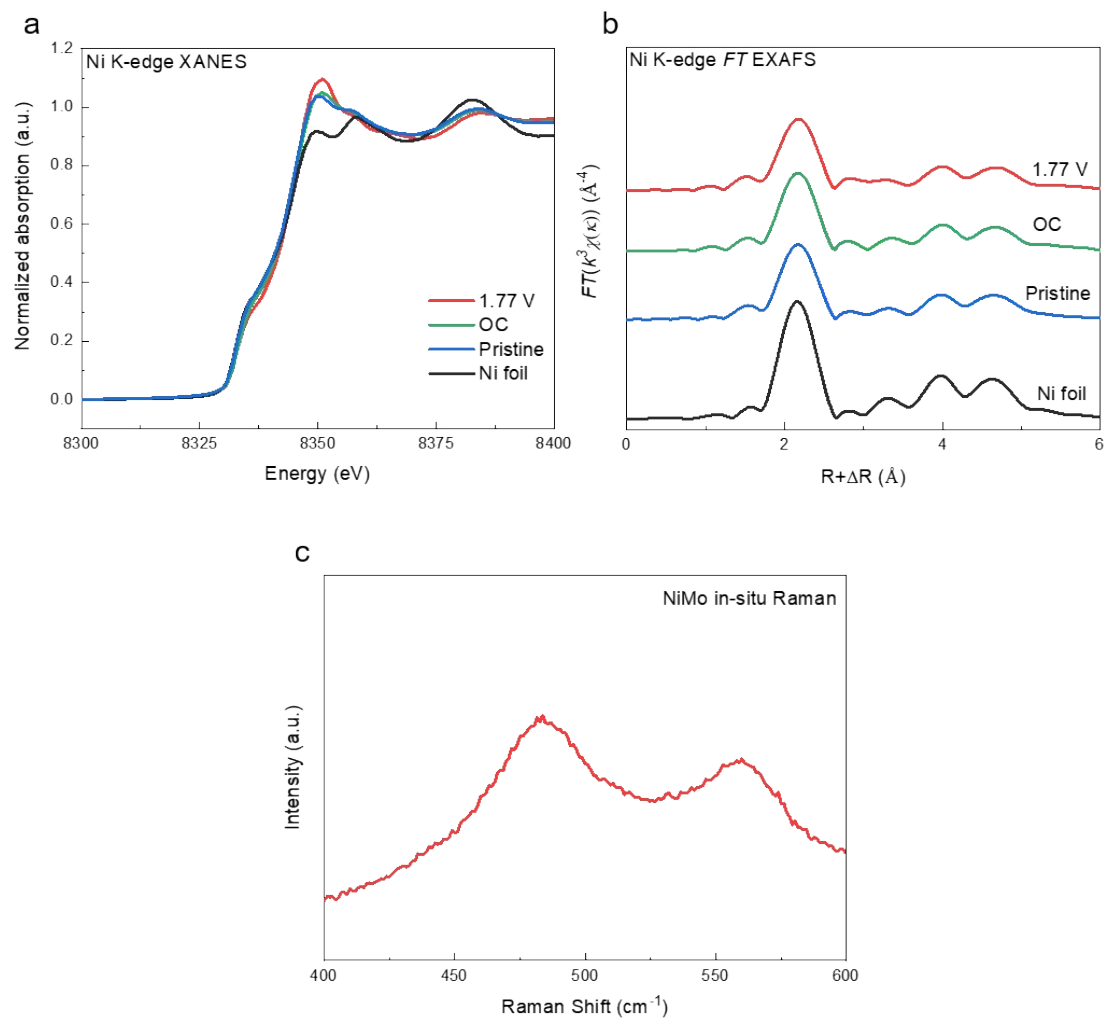

Figure S8. Elemental quantification results of the pristine and the reconstructed Fe$_1$-NiMo catalyst from ICP-OES, showing the dissolution of Mo.

1

2 **Figure S9. Semi-quantitative ratio of Fe to Ni from XPS depth-profile of the**

3 **reconstructed Fe$_1$-NiMo.** The rate of etching is $\sim$ 0.2 nm s^{-1}, indicating that Fe mainly

4 located at the top ~4 nm on the surface.

Figure S10. In-situ characterization of NiMo. a, b, XANES (**a**) and FT-EXAFS (**b**) of NiMo under different condition and Ni foil reference. **c,** In-situ Raman spectrum of NiMo under 1.47 V vs RHE. These results indicate that NiMo is also composed of metallic core and NiOOH shell under OER condition.
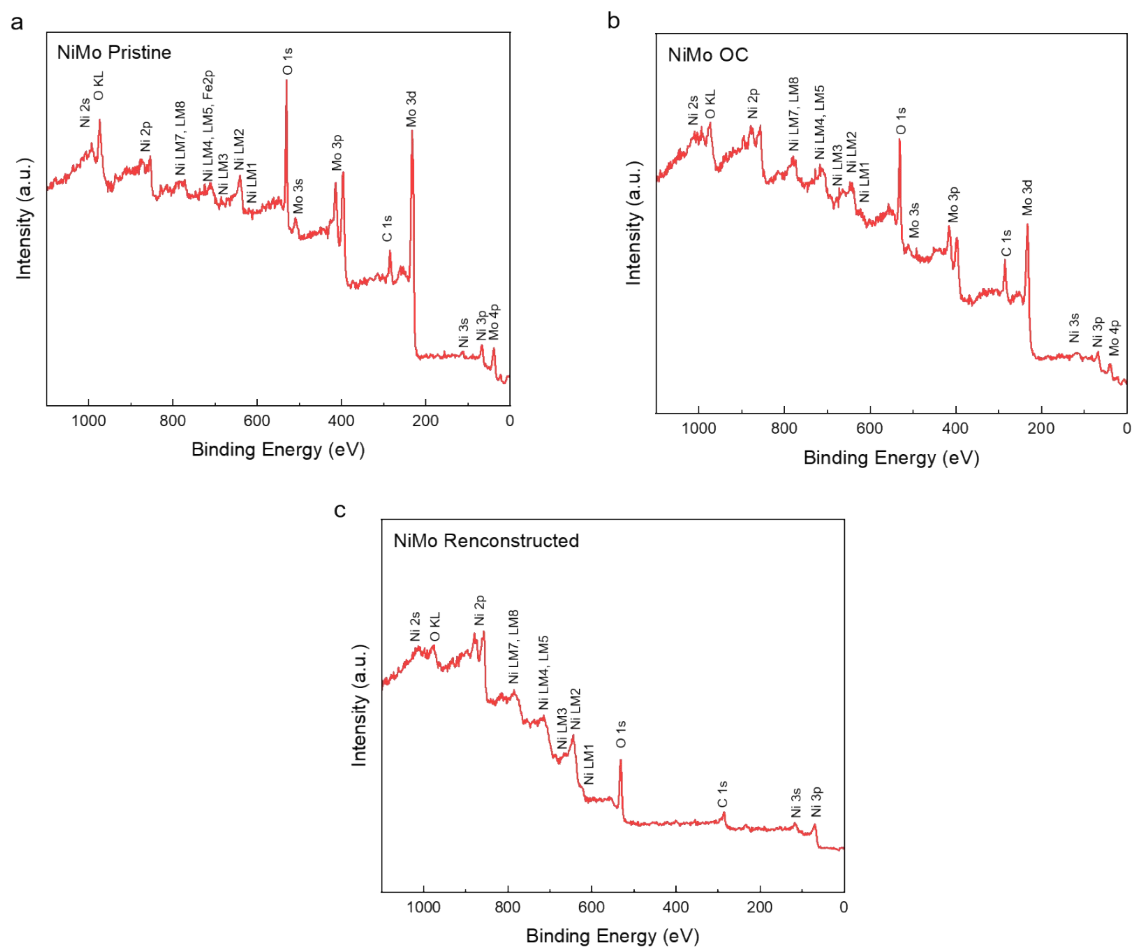
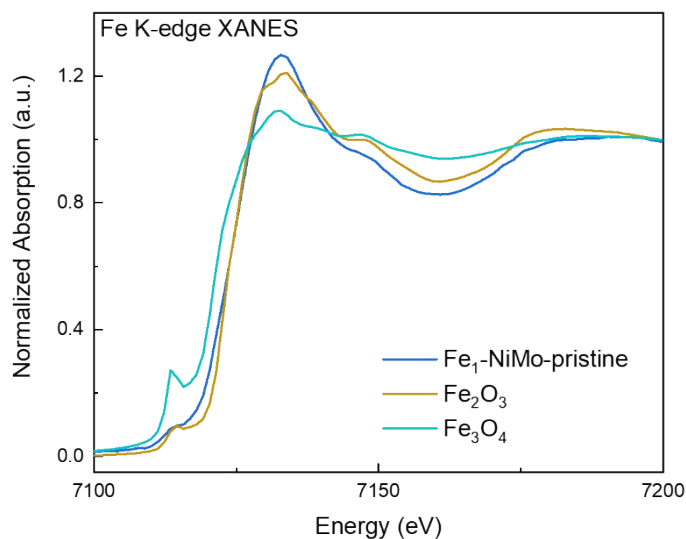**Figure S11. XPS survey spectra of pristine NiMo (a), NiMo after OC (b), NiMo after reconstructed under OER.** The rate of etching is ~ 0.2 nm s^{-1}.
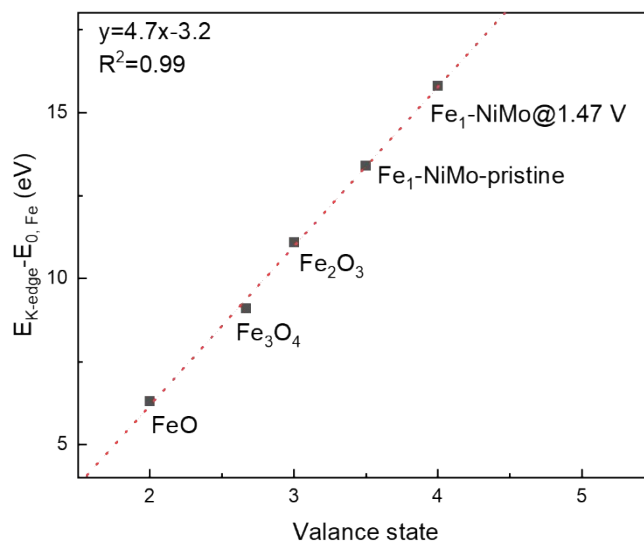

Figure S12. XANES spectra at Fe K-edge of pristine Fe$_1$-NiMo, Fe$_2$O$_3$ reference and

1 **Fe_3O_4 reference.** The absorption edge position of Fe_1-NiMo is closed to Fe_2O_3, indicating

2 the valance state of Fe in Fe_1-NiMo is closed to Fe^{3+}.

3

4

5 **Figure S13. Linear exportation of Fe K-edge position of Fe_1-NiMo and reference**

6 **compounds.** This result indicates that Fe in Fe_1-NiMo is oxidized to a Fe^{4+}.

7

8
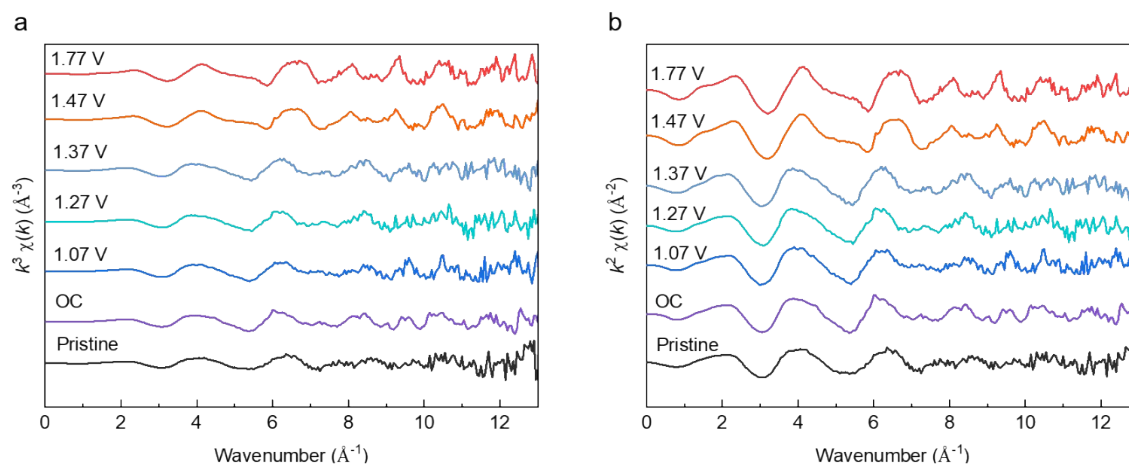
9 **Figure S14. The in-situ k^3-weighted (a), and k^2-weighted (b), EXAFS spectra at Fe K-**

10 **edge of Fe_1-NiMo.**

11
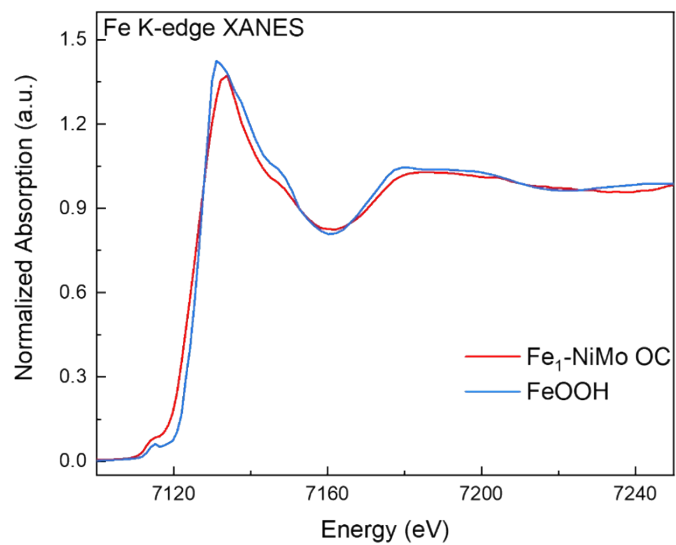
Figure S15. Comparison of XANES at Fe K-edge of Fe₁-NiMo under OC conditions and FeOOH. The XANES of Fe₁-NiMo shows a higher pre-edge peak and a lower intensity of the white line peak compared to that of FeOOH.
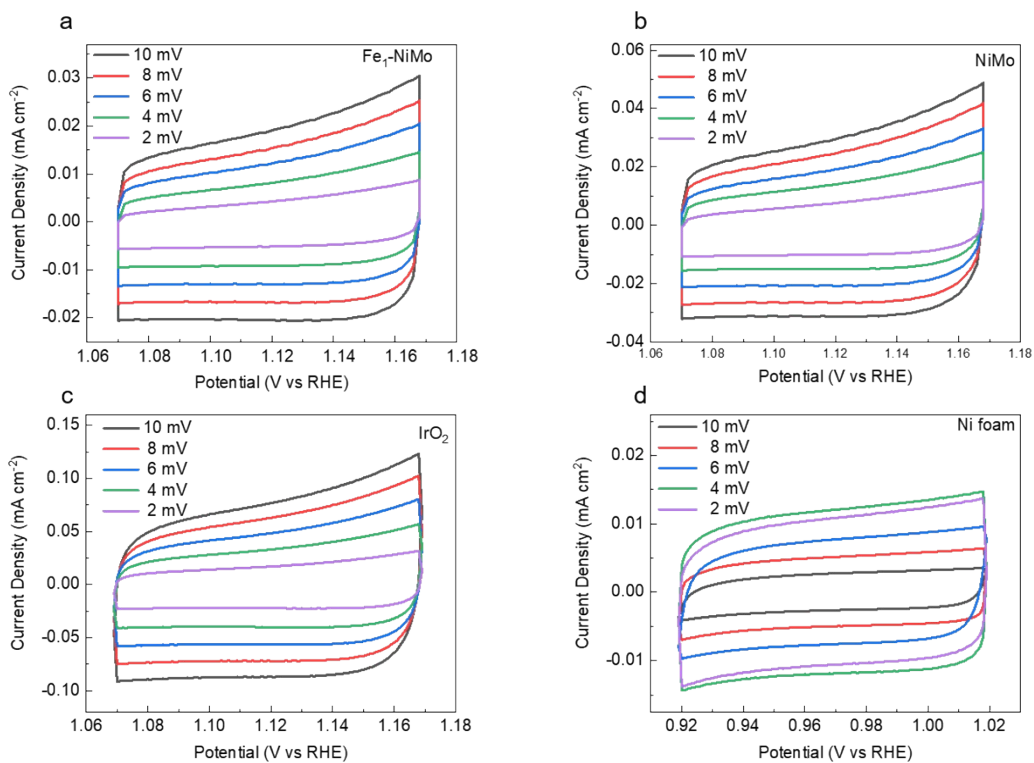
Figure S16. CV curves of (a)Fe$_1$-NiMo, (b) NiMo, (c) IrO$_2$, and (d) Ni foam in 1.0 M KOH electrolyte.
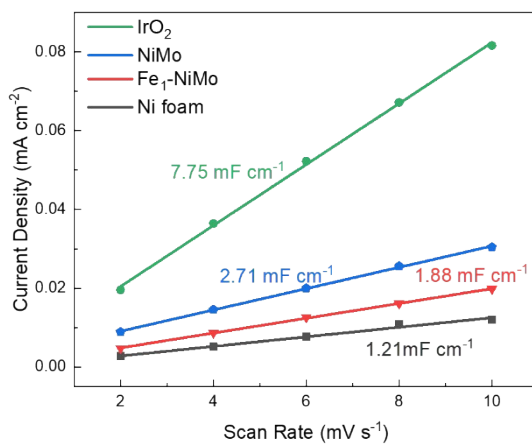
Figure S17. Electrochemical double layer capacities of Fe$_1$-NiMo, NiMo, IrO$_2$, and Ni foam.
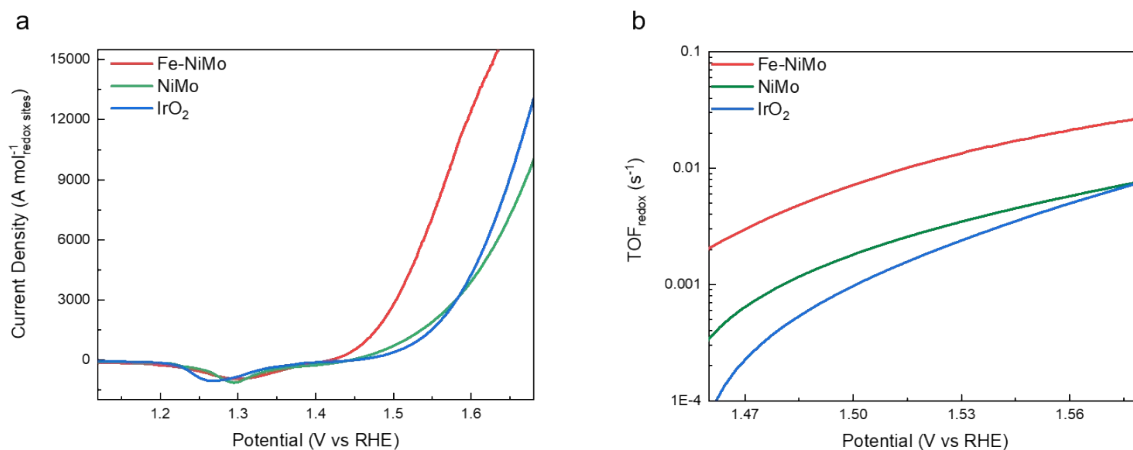
Figure S18. Polarization curves (a), and TOFs (b) normalized by the areas of the redox peaks. This calculation is based on the assumption that the reducing reaction is a single electron reaction and all the metal atoms that participated in the reducing reaction are the active sites.
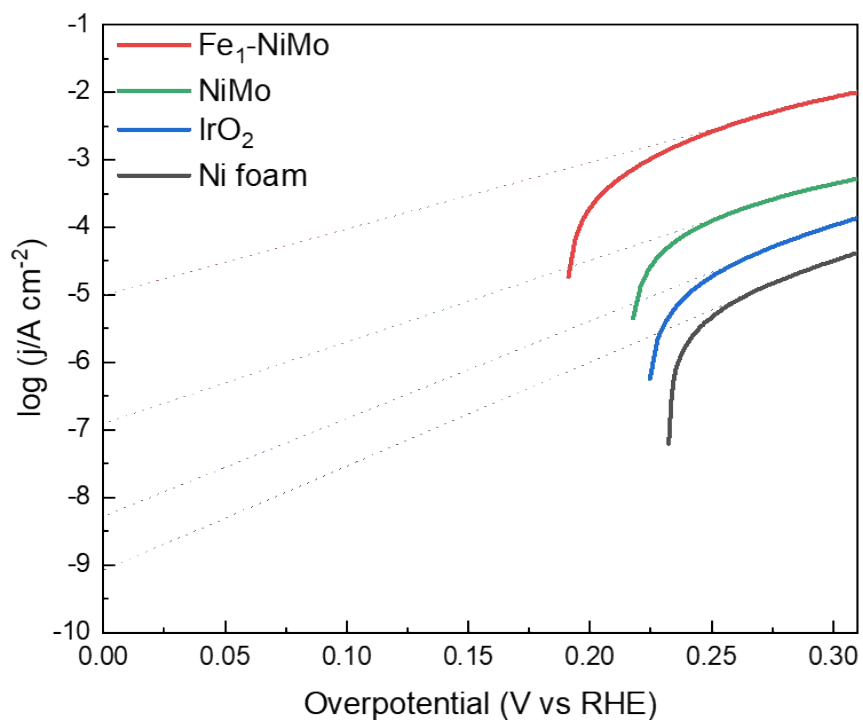
Figure S19. Exchange current densities of Fe$_1$-NiMo, NiMo, IrO$_2$, and Ni foam. These

1   results indicate Fe$_1$-NiMo process highest activity.

2
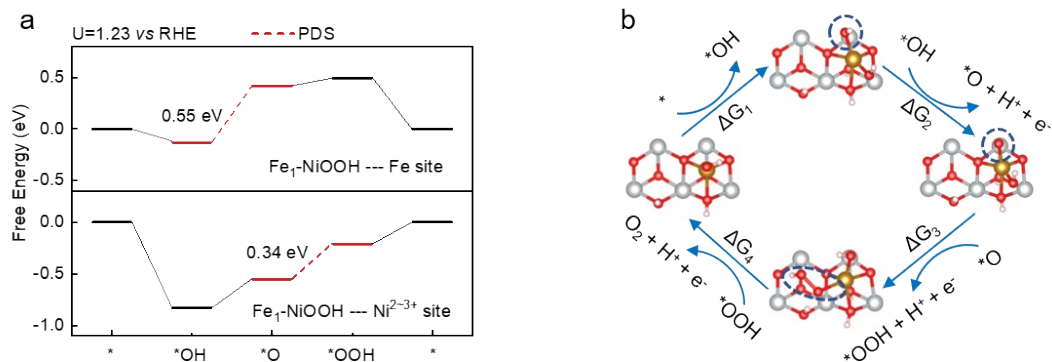
3

4 **Figure S20. OER activity of Fe site in Fe$_1$-NiMo. a,** Free energy diagram of OER on the

5   Fe site. **b,** OER cycles for Fe site. (Orange, Fe; grey, Ni; red, O; white, H)

6
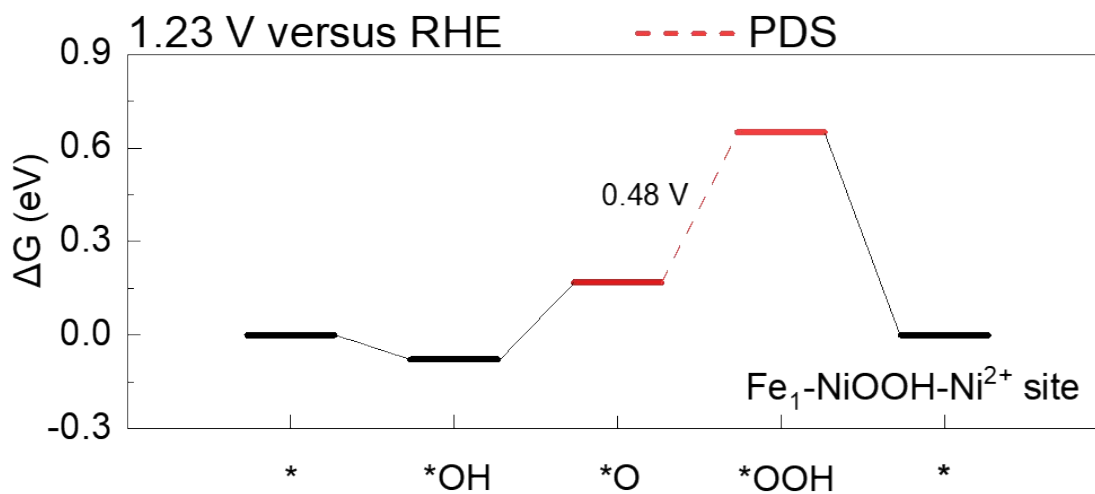
7

8 **Figure S21. Calculated free energy diagram of OER on the Ni^{2+} site**.

9

1
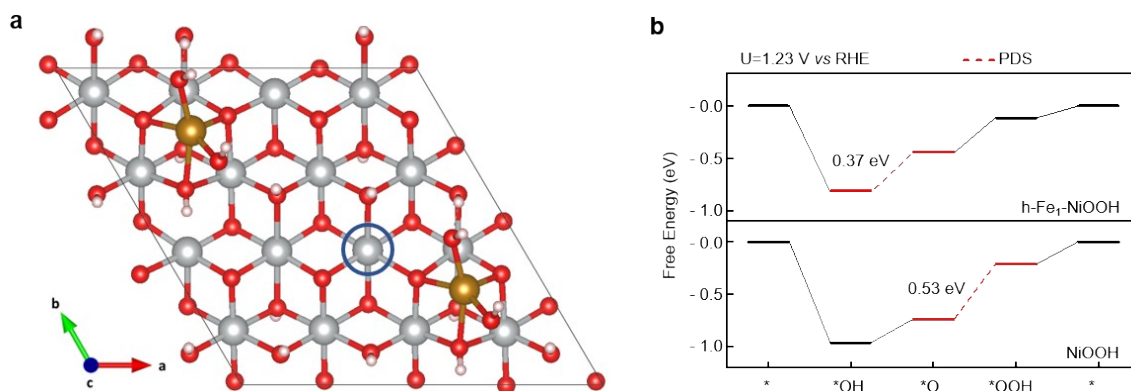
Figure S22. OER activity of h-Fe$_1$-NiOOH with a Ni/Fe ratio of 8:1. (a) Atomic model
of Fe$_1$-NiOOH with two mononuclear Fe. The Ni$^{(2\sim3)+}$ with a magnetic moments of 1.7 μ_B
is labeled by a blue cycle. The magnetic moments of Fe is 4.2 μ_B, corresponding to Fe^{4+}. (b)
Free energy diagram of OER on the Ni$^{(2\sim3)+}$ site.

6

7
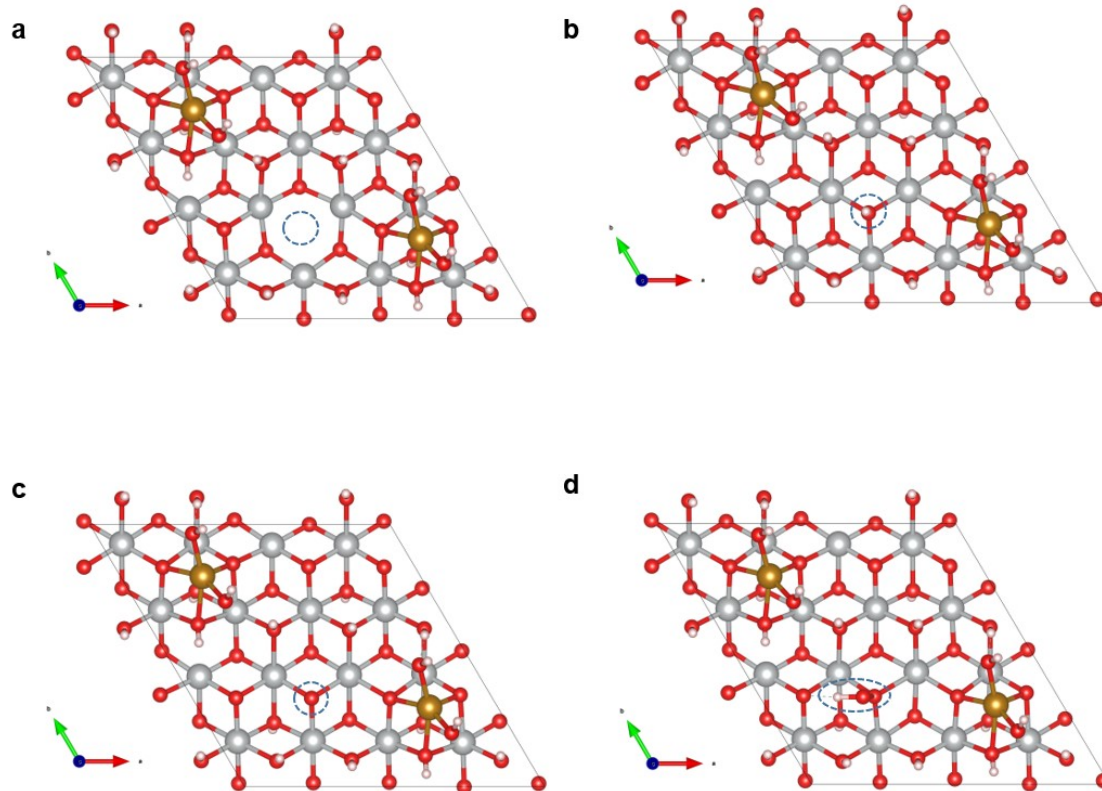
Figure S23. Structure of h-Fe$_1$-NiOOH at * (a), *OH (b), *O (c), *OOH (d) step.

9
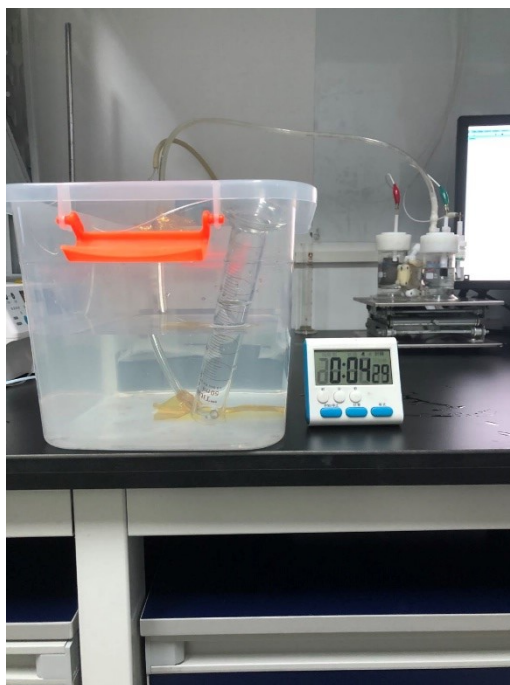
1

2   **Figure S24. A home-made setup for the test of Faraday efficiency**.

3
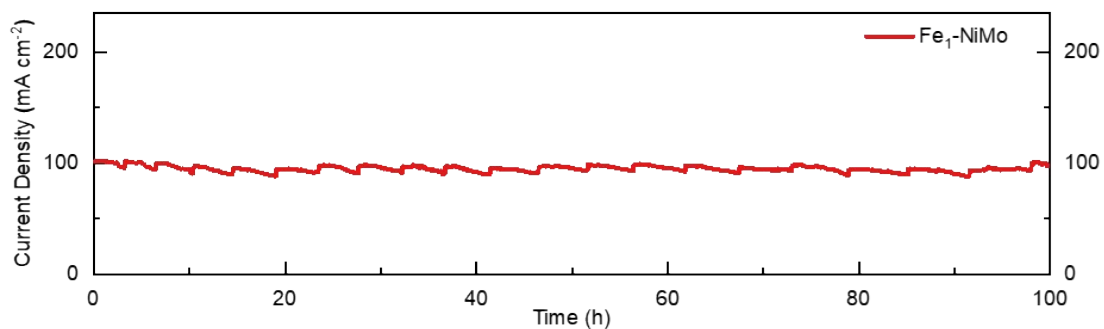
4

5   **Figure S25. Stability test of Fe$_1$-NiMo.** This result demonstrates the high stability of Fe$_1$-

6   NiMo for oxygen evolution. This data is obtained at 1.569 V vs RHE without iR correction.

7   And the resistance of solution is 1.065 Ω.

1

2
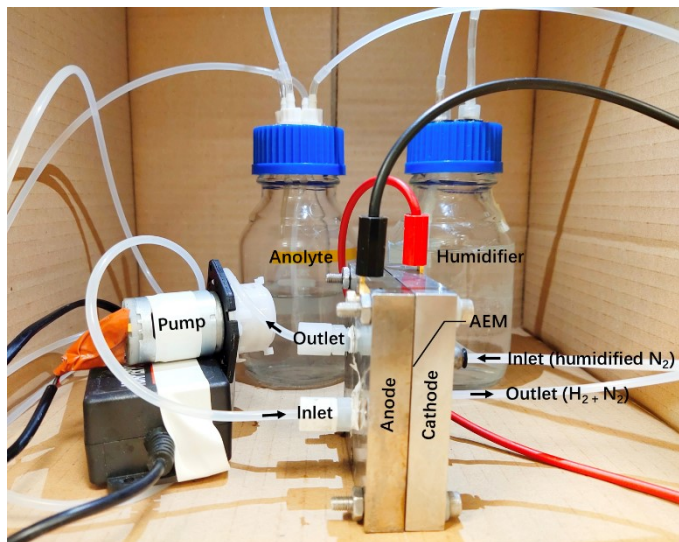
Figure S26. Setup for measuring the performance of Fe$_1$-NiMo in membrane

electrode assembly.

5

Table S1. Semi-quantitative results of XPS depth-profile of as pristine Fe$_1$-NiMo.

	Element	Fe	Ni	Mo
Concentration (at%)	Before etching	1.79±0.19	25.01±2.86	73.19±2.90
	10s etching[a]	0.10±0.14	28.53±4.65	71.37±4.52

[a]The rate of etching in this work is ~0.2 nm s^{-1}

8

Table S2. Semi-quantitative results of XPS depth-profile of reconstructed Fe$_1$-NiMo.

	Element	Fe	Ni	Mo
Concentration (at%)	Before etching	11.36±2.51	88.52±2.36	0.12±0.16
	10s etching	1.48±1.44	80.34±1.89	18.27±1.18
	20s etching	0.31±0.44	94.12±1.10	5.57±0.67

10

Table S3. Structural parameters of Fe$_1$-NiMo as well as reference samples extracted

from the Fe K-edge EXAFS fitting. ($S_0{}^2$=0.76)

Name	Atomic scatter	Coordination Number	Interatomic distance (Å)	ΔE_0 (eV)	Debye-Waller factor $(10^{-3} \times Å^2)$	R factor
Fe$_2$O$_3$	Fe-O	6.00	2.03±0.13	-2.731	12.4	0.0056
Fe$_1$-NiMo-Pristine	Fe-O	4.74±0.95	2.02±0.13	0.117	11.8	0.0070
Fe$_1$-NiMo-OC	Fe-O	4.87±0.97	2.01±0.03	-0.895	6.75	0.013
	Fe-Ni	2.92±0.58	3.09±0.07	-4.531	14.08	
Fe$_1$-NiMo-1.47 V	Fe-O	5.32±1.06	1.94±0.09	-2.129	8.03	0.0032
	Fe-Ni	3.19±0.64	2.86±0.04	-9.97	9.18	

1 The k^3-weighted EXAFS of Fe K-edge was Fourier transformed to R space using a Hanning

2 window (dk = 1.0 Å^{-1}) in k-space between 2.670 and 12.085 Å^{-1}. The amplitude-reduction

3 factor S_0^2 was determined by fitting the experimental Fe$_2$O$_3$ powder data.

4

5

6 **Table S4. A comparison of the OER activity in 1M KOH that normalized by ECSA**

Catalysts	Overpotential at 1 mA cm$^{-2}_{ECSA}$ （mV）	reference

Fe$_1$-NiMo	**225**	**This work**
Ni$_{83}$Fe$_{17}$-ONCAs	215	[17]
Ni$_{0.8}$Fe$_{0.2}$-AHNA	234	[18]
Fe-doped Ni(OH)$_2$	259	[19]
Se-FeOOH	324	[20]
EA-FCCA	257	[21]
NR-Ni(OH)$_2$	232	[22]
Fe-Co$_3$O$_4$	>300	[23]
Co$_{0.85}$Se-20	248	[24]
CuO nanoparticles	340	[25]

1

2 **Table S5.** Magnetic Moment of Ni in Fe$_1$-NiOOH and NiOOH at different stage of OER

3 process.

Catalyst	Magnetic Moment in corresponding stage (μ_B)			
	*	*OH	*O	*OOH
Fe$_1$-NiOOH	1.7	1.7	1.4	1.7
NiOOH	1.7	1.7	1.1	1.7
h-Fe$_1$-NiOOH	1.7	1.7	1.4	1.7

4

5 **Table S6. A comparison of the OER performance in 1M KOH that normalized by**

6 **geometry area.**

Material	Current density (mA cm^{-2})	Overpotential (mV)	Reference
Fe$_1$-NiMo	**10**	**202**	**This**
	50	**227**	**work**
	100	**245**	
	500	**315**	
	1000	**378**	
Fe-doped β-Ni(OH)2	10	219	[19]
(Ni$_x$Fe$_{1-x}$)$_2$P	20	219	[26]
2D amorphous FePO$_4$	10	218	[27]
	300	270	
(NiFe)$_2$P(O) nano cube arrays	10	150	[28]
	800	530	
Co–Ni–Se/C/NF	30	270	[29]
	50	300	
NiCoP-NWAs nanocone arrays	20	270	[30]
	100	370	
2D NiCoFe phosphate NSs/N	10	240	[31]
Ni$_{0.65}$Ga$_{0.30}$Fe$_{0.05}$/NF	10	200	[32]
NiFe/NiCo$_2$O$_4$	1200	340	[33]
Ni$_{0.8}$Fe$_{0.2}$-AHNA	10	193	[18]

	50	221	
	100	230	
	500	248	
	1000	258	
Se-(NiCo)S/OH	10	155	[34]
	120	240	
Ni-Fe-OH@Ni$_3$S$_2$/NF	10	165	[35]
	100	240	
	500	370	
	1000	469	
	1500	565	
Ni$_3$FeN-NPs	10	280	[36]
	900	970	
FeCoNi-HNTAs	10	184	[37]
	10	204	
Co-doped FeNi carbonate hydroxide	50	216	[38]
	100	225	
	500	254	
Nanostructured NiFe (oxy)hydroxide	500	261	[39]
FeNiMo oxyhydroxide	10	180	[40]
Fe(PO$_3$)$_2$/Ni$_2$P	500	265	[41]
Se doped FeOOH	500	348	[20]

Ni$_x$Fe$_{1-x}$Se$_2$-derived oxide	10	195	[42]
	265	250	
NiMoN@NiFeN	100	277	[43]
	500	377	
NiMoO$_x$/NiMoS	10	186	[44]
	100	225	
	500	278	
	1000	334	
NiFe coordination polymer	10	188	[45]
	50	214	
	100	234	
	150	249	
	200	260	
FeP/Ni$_2$P	10	154	[45]
	690	281	
	1000	293	
	277	1277	
NiVIr-LDH	10	180	[46]
	100	272	
NiFe-nanomeshes in graphene-like film	100	208	[47]
	500	253	
	1000	270	
3D-LDH @ Ni foam	50	239	[48]

100	252	
500	300	
1000	340	

1

2 **Table S7. Elemental analysis of the electrolyte tested with Fe₁-NiMo after the**

3 **reaction.**

Element	Fe	Ni	Mo
Concentration (mg/L)	ND[a]	ND	466.513±8.167

4 **[a]ND Stands for below the detection limit of our facility (0.002 mg/L of Fe, 0.008**

5 **mg/L of Ni, and 0.004 mg/L of Mo).**

6

7 **Table S8. Elemental analysis of Fe₁-NiMo and NiMo after the reaction**

	element	Fe	Ni	Mo
Concentration (wt%)	Fe₁-NiMo	1.49	60.06	4.99
	NiMo	0.02[a]	71.76	5.13

8 [a]The trace amount of Fe is came from the pollution in the experiment.

9

Supplementary Reference

1.   Newville BRM. ATHENA, ARTEMIS, HEPHAESTUS: data analysis for X-ray absorption spectroscopy using IFEFFIT *Journal of Synchrotron Radiation* 2005, **12:** 537-541.

2.   Rehr JJ, Albers RC. Theoretical approaches to x-ray absorption fine structure. *Reviews of Modern Physics* 2000, **72**(3)**:** 621-654.

3.   Funke H, Scheinost AC, Chukalina M. Wavelet analysis of extended x-ray absorption fine structure data. *Phys. Rev. B* 2005, **71**(9).

4.   McCrory CCL, Jung S, Ferrer IM, Chatman SM, Peters JC, Jaramillo TF. Benchmarking Hydrogen Evolving Reaction and Oxygen Evolving Reaction Electrocatalysts for Solar Water Splitting Devices. *J. Am. Chem. Soc.* 2015, **137**(13)**:** 4347-4357.

5.   McCrory CCL, Jung S, Peters JC, Jaramillo TF. Benchmarking Heterogeneous Electrocatalysts for the Oxygen Evolution Reaction. *J. Am. Chem. Soc.* 2013, **135**(45)**:** 16977-16987.

6.   Kresse G, Hafner J. Ab initio molecular dynamics for liquid metals. *Physical review B* 1993, **47**(1)**:** 558.

7.   Kresse G, Hafner J. Ab initio molecular-dynamics simulation of the liquid-metal–amorphous-semiconductor transition in germanium. *Physical Review B* 1994, **49**(20)**:** 14251.

8.   Kresse G, Furthmüller J. Efficient iterative schemes for ab initio total-energy calculations using a plane-wave basis set. *Physical review B* 1996, **54**(16)**:** 11169.

9.   Perdew JP, Burke K, Ernzerhof M. Generalized Gradient Approximation Made Simple. *Phys Rev Lett* 1996, **77**(18)**:** 3865-3868.

10.   Blöchl PE. Projector augmented-wave method. *Physical review B* 1994, **50**(24)**:** 17953.

11. Grimme S, Antony J, Ehrlich S, Krieg H. A consistent and accurate ab initio parametrization of density functional dispersion correction (DFT-D) for the 94 elements H-Pu. *The Journal of chemical physics* 2010, **132**(15)**:** 154104.

12. Grimme S, Ehrlich S, Goerigk L. Effect of the damping function in dispersion corrected density functional theory. *J. Comput. Chem.* 2011, **32**(7)**:** 1456-1465.

13. Dudarev SL, Botton GA, Savrasov SY, Humphreys CJ, Sutton AP. Electron-energy-loss spectra and the structural stability of nickel oxide: An LSDA+U study. *Phys. Rev. B* 1998, **57**(3)**:** 1505-1509.

14. Zhou Y, López N. The Role of Fe Species on NiOOH in Oxygen Evolution Reactions. *ACS Catal.* 2020, **10**(11)**:** 6254-6261.

15. Rossmeisl J, Logadottir A, Nørskov JK. Electrolysis of water on (oxidized) metal surfaces. *Chemical Physics* 2005, **319**(1-3)**:** 178-184.

16. Rossmeisl J, Qu ZW, Zhu H, Kroes GJ, Nørskov JK. Electrolysis of water on oxide surfaces. *J Electroanal Chem* 2007, **607**(1-2)**:** 83-89.

17. Liu P, Chen B, Liang C, Yao W, Cui Y, Hu S*, et al.* Tip-Enhanced Electric Field: A New Mechanism Promoting Mass Transfer in Oxygen Evolution Reactions. *Adv. Mater.* 2021, **33**(9)**:** 2007377.

18. Liang C, Zou P, Nairan A, Zhang Y, Liu J, Liu K*, et al.* Exceptional performance of hierarchical Ni–Fe oxyhydroxide@NiFe alloy nanowire array electrocatalysts for large current density water splitting. *Energy Environ. Sci.* 2020, **13**(1)**:** 86-95.

19. Kou T, Wang S, Hauser JL, Chen M, Oliver SRJ, Ye Y*, et al.* Ni Foam-Supported Fe-Doped β-Ni(OH)2 Nanosheets Show Ultralow Overpotential for Oxygen Evolution Reaction. *ACS Energy Lett.* 2019, **4**(3)**:** 622-628.

20. Niu S, Jiang W-J, Wei Z, Tang T, Ma J, Hu J-S*, et al.* Se-Doping Activates FeOOH for Cost-Effective and Efficient Electrochemical Water Oxidation. *J. Am. Chem. Soc.* 2019, **141**(17)**:** 7005-7013.

21. Zhang N, Feng X, Rao D, Deng X, Cai L, Qiu B*, et al.* Lattice oxygen activation

35

enabled by high-valence metal sites for enhanced water oxidation. *Nat. Commun.* 2020, **11**(1)**:** 4066.

22. Wang XP, Wu HJ, Xi SB, Lee WSV, Zhang J, Wu ZH*, et al.* Strain stabilized nickel hydroxide nanoribbons for efficient water splitting. *Energy Environ. Sci.* 2020, **13**(1)**:** 229-237.

23. Zhang SL, Guan BY, Lu XF, Xi S, Du Y, Lou XW. Metal Atom-Doped Co 3 O 4 Hierarchical Nanoplates for Electrocatalytic Oxygen Evolution. *Adv. Mater.* 2020, **32**(31)**:** 2002235.

24. Zhang J, Xu Q, Hu Y, Jiang H, Li C. Selenium vacancy triggered atomic disordering of $Co_{0.85}$Se nanoparticles towards a highly-active electrocatalyst for water oxidation. *Chem. Commun.* 2020, **56**(92)**:** 14451-14454.

25. Huan TN, Rousse G, Zanna S, Lucas IT, Xu X, Menguy N*, et al.* A Dendritic Nanostructured Copper Oxide Electrocatalyst for the Oxygen Evolution Reaction. *Angew. Chem. Int. Ed.* 2017, **56**(17)**:** 4792-4796.

26. Yu J, Cheng G, Luo W. Hierarchical NiFeP microflowers directly grown on Ni foam for efficient electrocatalytic oxygen evolution. *J. Mater. Chem. A* 2017, **5**(22)**:** 11229-11235.

27. Yang L, Guo Z, Huang J, Xi Y, Gao R, Su G*, et al.* Vertical Growth of 2D Amorphous FePO 4 Nanosheet on Ni Foam: Outer and Inner Structural Design for Superior Water Splitting. *Adv. Mater.* 2017, **29**(46)**:** 1704574.

28. Xi W, Yan G, Lang Z, Ma Y, Tan H, Zhu H*, et al.* Oxygen-Doped Nickel Iron Phosphide Nanocube Arrays Grown on Ni Foam for Oxygen Evolution Electrocatalysis. *Small* 2018, **14**(42)**:** 1802204.

29. Ming F, Liang H, Shi H, Xu X, Mei G, Wang Z. MOF-derived Co-doped nickel selenide/C electrocatalysts supported on Ni foam for overall water splitting. *J. Mater. Chem. A* 2016, **4**(39)**:** 15148-15155.

30. Li J, Wei G, Zhu Y, Xi Y, Pan X, Ji Y, *et al.* Hierarchical NiCoP nanocone arrays supported on Ni foam as an efficient and stable bifunctional electrocatalyst for overall water splitting. *J. Mater. Chem. A* 2017, **5**(28)**:** 14828-14837.

31. Sial MAZG, Lin H, Wang X. Microporous 2D NiCoFe phosphate nanosheets supported on Ni foam for efficient overall water splitting in alkaline media. *Nanoscale* 2018, **10**(27)**:** 12975-12980.

32. Zai SF, Dong AQ, Li J, Wen Z, Yang CC, Jiang Q. Low-crystallinity mesoporous NiGaFe hydroxide nanosheets on macroporous Ni foam for high-efficiency oxygen evolution electrocatalysis. *J. Mater. Chem. A* 2021, **9**(10)**:** 6223-6231.

33. Xiao C, Li Y, Lu X, Zhao C. Bifunctional Porous NiFe/NiCo2O4/Ni Foam Electrodes with Triple Hierarchy and Double Synergies for Efficient Whole Cell Water Splitting. *Adv. Funct. Mater.* 2016, **26**(20)**:** 3515-3523.

34. Hu C, Zhang L, Zhao Z-J, Li A, Chang X, Gong J. Synergism of Geometric Construction and Electronic Regulation: 3D Se-(NiCo)S$_x$/(OH)$_x$Nanosheets for Highly Efficient Overall Water Splitting. *Adv. Mater.* 2018, **30**(12)**:** 1705538.

35. Zou X, Liu Y, Li G-D, Wu Y, Liu D-P, Li W, *et al.* Ultrafast Formation of Amorphous Bimetallic Hydroxide Films on 3D Conductive Sulfide Nanoarrays for Large-Current-Density Oxygen Evolution Electrocatalysis. *Adv. Mater.* 2017, **29**(22)**:** 1700404.

36. Jia X, Zhao Y, Chen G, Shang L, Shi R, Kang X, *et al.* Ni$_3$FeN Nanoparticles Derived from Ultrathin NiFe-Layered Double Hydroxide Nanosheets: An Efficient Overall Water Splitting Electrocatalyst. *Advanced Energy Materials* 2016, **6**(10)**:** 1502585.

37. Li H, Chen S, Zhang Y, Zhang Q, Jia X, Zhang Q, *et al.* Systematic design of superaerophobic nanotube-array electrode comprised of transition-metal sulfides for overall water splitting. *Nat. Commun.* 2018, **9**(1)**:** 2452.

38. Qi Y, Wang Q, Wang X, Liu Z, Zhao X, Yang E. Self-supported Co-doped FeNi

carbonate hydroxide nanosheet array as a highly efficient electrocatalyst towards the oxygen evolution reaction in an alkaline solution. *Nanoscale* 2019, **11**(22)**:** 10595-10602.

39. Zhong D, Zhang L, Li C, Li D, Wei C, Zhao Q*, et al.* Nanostructured NiFe (oxy)hydroxide with easily oxidized Ni towards efficient oxygen evolution reactions. *J. Mater. Chem. A* 2018, **6**(35)**:** 16810-16817.

40. Zhang B, Wang L, Cao Z, Kozlov SM, García De Arquer FP, Dinh CT*, et al.* High-valence metals improve oxygen evolution reaction performance by modulating 3d metal oxidation cycle energetics. *Nat. Catal.* 2020, **3**(12)**:** 985-992.

41. Zhou H, Yu F, Sun J, He R, Chen S, Chu C-W*, et al.* Highly active catalyst derived from a 3D foam of $Fe(PO_3)_2Ni_2P$ for extremely efficient water oxidation. *Proc. Natl. Acad. Sci.* 2017, **114**(22)**:** 5607-5611.

42. Xu X, Song F, Hu X. A nickel iron diselenide-derived efficient oxygen-evolution catalyst. *Nat. Commun.* 2016, **7**(1)**:** 12324.

43. Yu L, Zhu Q, Song S, McElhenny B, Wang D, Wu C*, et al.* Non-noble metal-nitride based electrocatalysts for high-performance alkaline seawater electrolysis. *Nat. Commun.* 2019, **10**(1)**:** 5106.

44. Zhai P, Zhang Y, Wu Y, Gao J, Zhang B, Cao S*, et al.* Engineering active sites on hierarchical transition bimetal oxides/sulfides heterostructure array enabling robust overall water splitting. *Nat. Commun.* 2020, **11**(1)**:** 5462.

45. Li W, Li F, Yang H, Wu X, Zhang P, Shan Y*, et al.* A bio-inspired coordination polymer as outstanding water oxidation catalyst via second coordination sphere engineering. *Nat. Commun.* 2019, **10**(1)**:** 5074.

46. Wang D, Li Q, Han C, Lu Q, Xing Z, Yang X. Atomic and electronic modulation of self-supported nickel-vanadium layered double hydroxide to accelerate water splitting kinetics. *Nat. Commun.* 2019, **10**(1)**:** 3899.

47. Zhang J, Jiang WJ, Niu S, Zhang H, Liu J, Li H*, et al.* Organic Small Molecule

Activates Transition Metal Foam for Efficient Oxygen Evolution Reaction. *Adv. Mater.* 2020, **32**(11)**:** 1906015.

48. Liu Y, Liang X, Gu L, Zhang Y, Li G-D, Zou X*, et al.* Corrosion engineering towards efficient oxygen evolution electrodes with stable catalytic activity for over 6000 hours. *Nat. Commun.* 2018, **9**(1)**:** 2609.